

Simultaneously Powering and Controlling Many Actuators with a Clinical MRI Scanner

Aaron Becker, Ouajdi Felfoul, and Pierre E. Dupont

Abstract—Actuators that are powered, imaged, and controlled by Magnetic Resonance (MR) scanners offer the potential of inexpensively providing wireless control of MR-guided robots. Similar to traditional electric motors, the MR scanner acts as the stator and generates propulsive torques on an actuator rotor containing one or more ferrous particles. The MR scanner can control three orthogonal gradient fields. Prior work demonstrated control of a single actuator rotor. This paper proposes and demonstrates independent, simultaneous control of n rotors. The controller relies on inhomogeneity between rotors, such as ensuring no rotor axes are parallel. This paper provides easily-implemented velocity and position controllers with global asymptotic convergence, and optimization techniques for implementation. Code for simulations and control laws is available online.

I. INTRODUCTION

Robotics offers important contributions to image-guided, minimally invasive surgery. Among imaging techniques, MRI has several advantages. MRI provides high resolution soft-tissue imaging and does not use ionizing radiation.

MR image-guided procedures, however, pose several challenges for robotics [1]–[5]. First, all ferrous materials create imaging artifacts. Ferrous materials must be isolated from the imaging region of interest. Moreover, the magnetic fields used in an MRI induce forces on any ferrous materials in the robot and turn these materials into strong magnetic dipoles that exert forces on each other. MRI gradients induce current in any conducting materials, which can generate dangerous amounts of heat and also exert forces.

Despite these challenges, there are a number of recent innovations demonstrating tetherless and inexpensive actuation imaged, powered, and controlled using MRI. Martel et al. demonstrated in vivo motion control of a mm-scale particle in the carotid artery of swine [3]. Vartholomeos et al. designed a single-DOF MRI-powered actuator for use as a tetherless biopsy robot [4]. This was extended to closed-loop control of a single rotor in [5]. Since such results require only scanner software and inexpensive actuator components, dissemination of MRI-based robotic technology has the potential to be rapid and inexpensive.

While this prior work has demonstrated control of a single particle or a single rotor, many clinical applications require multiple DOF. This is a challenge because the three orthogonal magnetic gradients of MRI scanners are applied

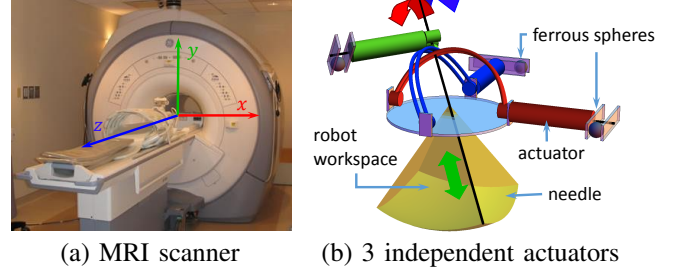


Fig. 1. This paper proves that n non-parallel rotors can be independently actuated by the same magnetic gradient field. The torque from these rotors could power multi-DOF robotic actuators running untethered inside an MRI bore such as (b), a biopsy robot inspired by [6] that can insert a needle and tilt the needle to a two DOF compound angle.

over the entire scanner bore, so the resulting control problem is underactuated. Techniques from nonlinear control theory must be used to demonstrate controllability and to derive control laws.

The contribution of this paper is to develop control techniques enabling independent control of large numbers of rotors. Section II describes an MRI actuator model and a multi-rotor control law. Section III examines multi-actuator system optimization. Section IV applies these principles to design a 3 DOF biopsy robot (Fig. 1), and Section V ends with concluding remarks.

II. MULTI-ROTOR CONTROL

A ferrous particle in the strong static field of an MRI becomes magnetized, and its magnetization magnitude asymptotically approaches the saturation magnetization \mathbf{M}_s per unit volume of the material. The MRI gradient coils produce a magnetic field $\mathbf{B}_g(t)$. This field exerts on the ferrous particle the force

$$\mathbf{F}(t) = v (\mathbf{M}_s \cdot \nabla) \mathbf{B}_g(t). \quad (1)$$

Here v is the magnetic volume of the material. The magnetic field $\mathbf{B}_g(t)$ is designed to produce three independent gradients:

$$[F_x, F_y, F_z]^T(t) = v M_{sz} \left[\frac{\partial B_{gz}}{\partial x}, \frac{\partial B_{gz}}{\partial y}, \frac{\partial B_{gz}}{\partial z} \right]^T(t) \quad (2)$$

Here it has been reasonably assumed that $M_{sz} \gg M_{sx}, M_{sy}$. These gradients apply three independent forces on any ferromagnetic spheres inside the MRI. This paper investigates rotors that constrain the i th ferromagnetic sphere to rotate about an axis \mathbf{a}_i with a moment arm of length r_i , as shown in Fig. 2. The rotor's configuration is fully described by

A. Becker, O. Felfoul, and P. E. Dupont are with the Department of Cardiovascular Surgery, Boston Children's Hospital and Harvard Medical School, Boston, MA, 02115 USA `first.name.lastname@childrens.harvard.edu`. This work was supported by the National Science Foundation under IIS-1208509 and by the Wyss Institute for Biologically Inspired Engineering.

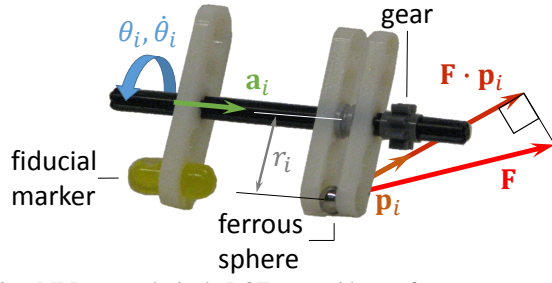


Fig. 2. MRI-powered, single-DOF rotor with gear for power transmission.

its angular position and velocity $[\theta_i, \dot{\theta}_i]^T$. The configuration space of all n rotors is $\mathbb{R}^{2 \times n}$, and the dynamic equations are

$$J_i \ddot{\theta}_i(t) = -b_i \dot{\theta}_i(t) - \tau_{f_i} - \tau_{\ell_i} + r_i \mathbf{F} \cdot \mathbf{p}_i(t) \quad (3)$$

Here J_i is the moment of inertia, b_i the coefficient of viscous friction, τ_{f_i} the summation of all non-viscous friction terms seen by the input, and τ_{ℓ_i} the load torque. The rotor torque is the magnetic force projected to a vector tangent to the ferrous sphere's positive direction of motion, $r_i \mathbf{F} \cdot \mathbf{p}_i(t)$. Actuator torque is maximized when $\mathbf{F}(t) = g_M V M_{sz} \text{sgn}(\mathbf{p}_i(t))$, where g_M is the maximum gradient.

There are two standard actuator control tasks: position and velocity control. The position control problem is to find inputs $\mathbf{F}(t)$ such that for any $\boldsymbol{\theta}(0)$ and $\boldsymbol{\theta}_{\text{goal}}$,

$$\lim_{t \rightarrow \infty} \sum_{i=1}^n \left\| \begin{bmatrix} \theta_i(t) \\ \dot{\theta}_i(t) \end{bmatrix} - \begin{bmatrix} \theta_{\text{goal},i} \\ 0 \end{bmatrix} \right\|_2 = 0. \quad (4)$$

This section starts with the simpler velocity control problem

$$\lim_{t \rightarrow \infty} \sum_{i=1}^n \left\| \dot{\theta}_i(t) - \omega_i \right\|_2 = 0, \quad (5)$$

where $\omega_i \in \mathbb{R}$ is the desired angular velocity of each rotor. After solving the velocity control problem in Sec. II-B, Section II-C uses an outer control loop to stabilize position.

A. Open-Loop Multi-Actuator Control

Before considering closed-loop control, it is worthwhile to determine what can be achieved in open-loop and to examine related performance limitations. In this context, one method to independently control multiple rotors uses the magnetic field gradients to make the rotors revolve around *orthogonal* axes. For notational simplicity, assume the rotors rotate about the world x, y, z axes. With $n \leq 3$ orthogonal rotors, open-loop control signals can rotate some rotors at constant velocities, and move the remaining rotors to steady-state positions. For instance, the control law

$$\nabla \mathbf{B}_g(t) = g_M [\cos(t), \sin(t), 0]^T \quad (6)$$

rotates the z -axis rotor in the positive direction at 1 rad/s and places the x and y rotors in steady-state positions.

To simultaneously rotate up to three orthogonal rotors, the gradient can be rotated at angular frequency ω around the vector $\boldsymbol{\phi} = \frac{[\phi_x, \phi_y, \phi_z]^T}{\sqrt{\phi_x^2 + \phi_y^2 + \phi_z^2}}$, where $\phi_i \in \{-1, 0, 1\}$ is the

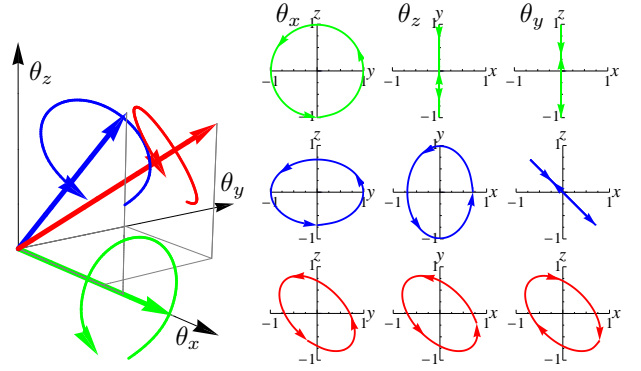


Fig. 3. The open-loop control law (7) for three orthogonal axes has 27 possible outputs corresponding with: only one rotor spinning (green), two rotors spinning (blue), all three spinning (red), or none spinning. At right are projections onto the three coordinate axes. See video attachment for experimental verification.

desired rotation of the i th axis. This gives the control law

$$\nabla \mathbf{B}_g(t) = g_M R_{\boldsymbol{\phi}, \omega t} \cdot \boldsymbol{\phi}_{\perp}. \quad (7)$$

Here $\boldsymbol{\phi}_{\perp}$ is a vector perpendicular to $\boldsymbol{\phi}$ and $R_{\boldsymbol{\phi}, \omega t}$ is the rotation matrix that rotates the angle ωt about the axis $\boldsymbol{\phi}$. Control law (7) with three orthogonal rotors has 27 possible outputs. Figure 3 shows three representative control inputs. The 2D projections show how rotating the magnetic field around different $\boldsymbol{\phi}$ vectors rotates one, two, or three rotors simultaneously.

As demonstrated in these examples, open-loop control has several limitations. For example, rotor velocities are coupled and position control is not possible. In addition, the approach is limited to at most three rotors since their axes must be orthogonal. Furthermore, as shown in the video attachment, cyclic slipping of the rotor due to applied load or perturbations is possible. Closed-loop control, described in the following subsection, can eliminate these limitations.

B. Closed-Loop Multi-Actuator Velocity Control

To enable robust, multi-axis control, a closed-loop controller can be designed using a control-Lyapunov function [7]. The control law selects the three magnetic gradients that decrease the sum of squared velocity error. There are configurations where no combination of velocity gradients will decrease this error, but it is always possible to apply a non-zero gradient without increasing the sum squared error. Any non-zero gradient will move the rotors to a new configuration where the error can be decreased. This technique is inspired by work on controlling many mobile robots with a uniform control signal [8]. For ease of analysis, simplified rotor dynamics will be used:

$$\ddot{\theta}_i(t) = \frac{r_i}{J_i} \mathbf{F}(t) \cdot \mathbf{p}_i(t). \quad (8)$$

In all simulations the full dynamic model (3) is used.

Given n non-parallel rotors and desired angular velocities ω_i , a suitable Lyapunov function can be defined as the sum squared velocity error:

$$V(\boldsymbol{\theta}, \dot{\boldsymbol{\theta}}, t) = \frac{1}{2} \sum_{i=1}^n \left(\omega_i - \dot{\theta}_i(t) \right)^2 \quad (9)$$

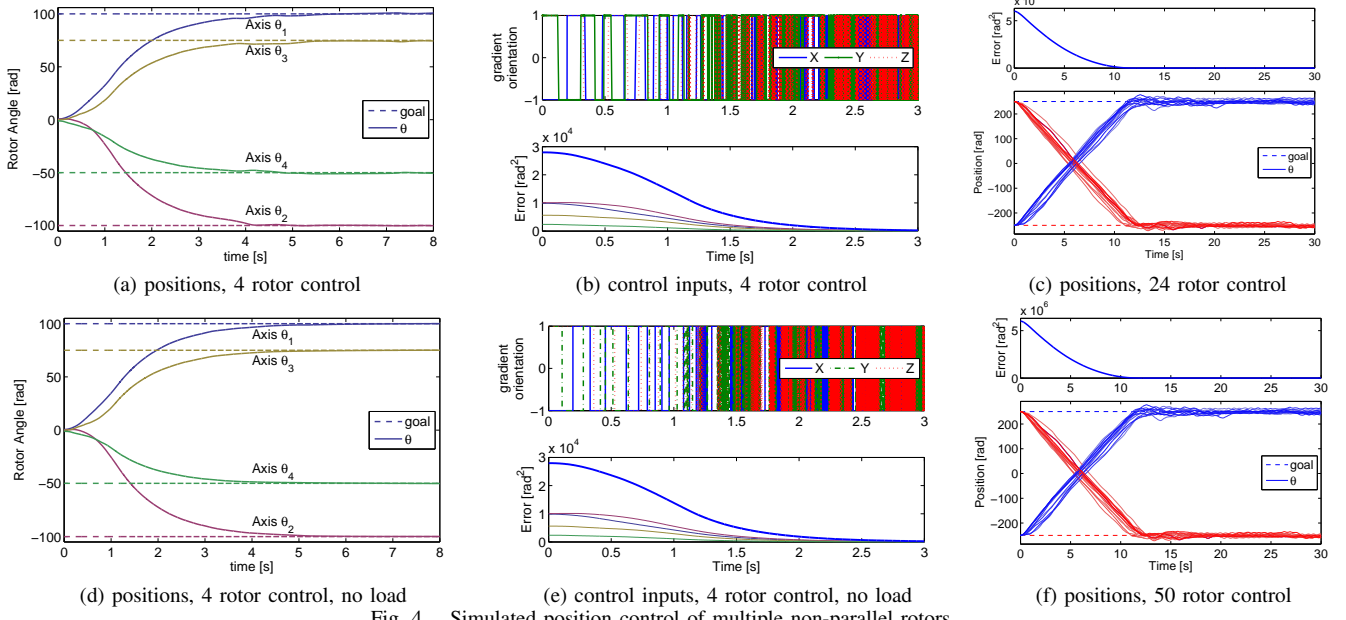


Fig. 4. Simulated position control of multiple non-parallel rotors.

$$\begin{aligned}\dot{V}(\boldsymbol{\theta}, \dot{\boldsymbol{\theta}}, t) &= \sum_{i=1}^n \left(\omega_i - \dot{\theta}_i(t) \right) \ddot{\theta}_i(t) \\ &= \mathbf{F}(t) \cdot \sum_{i=1}^n \left(\omega_i - \dot{\theta}_i(t) \right) \frac{r_i}{J_i} \mathbf{p}_i(t)\end{aligned}\quad (10)$$

Note that $V(\boldsymbol{\theta}, \dot{\boldsymbol{\theta}}, t)$ is positive definite, zero only at the target velocity, and radially unbounded. The following controller makes $\dot{V}(\boldsymbol{\theta}, \dot{\boldsymbol{\theta}}, t)$ negative semi-definite:

$$\mathbf{F}(t) = -g_M v_i M_{sz} \left(\sum_{i=1}^n \left(\omega_i - \dot{\theta}_i(t) \right) \frac{r_i}{J_i} \mathbf{p}_i(t) \right) \quad (11)$$

For such an $\mathbf{F}(t)$,

$$\dot{V}(\boldsymbol{\theta}, \dot{\boldsymbol{\theta}}, t) = -g_M v_i M_{sz} \left(\sum_{i=1}^n \left(\omega_i - \dot{\theta}_i(t) \right) \frac{r_i}{J_i} \mathbf{p}_i(t) \right)^2.$$

Notice that $\dot{V}(\boldsymbol{\theta}, \dot{\boldsymbol{\theta}}, t) \leq 0$, but there exists a subspace of $[\boldsymbol{\theta}, \dot{\boldsymbol{\theta}}]^\top$ where $\dot{V}(\boldsymbol{\theta}, \dot{\boldsymbol{\theta}}, t) = 0$. Because this derivative is negative semi-definite, the system is stable, but not necessarily asymptotically stable. To prove asymptotic stability requires proving that the invariant set contains only the rotors moving at the desired angular velocity.

Control law (11) is modified as follows:

$$\begin{aligned}\mathbf{f} &= \text{sgn} \left(- \sum_{i=1}^n \left(\omega_i - \dot{\theta}_i(t) \right) \frac{r_i}{J_i} \mathbf{p}_i(t) \right) \\ \mathbf{F}(t) &= g_M v_i M_{sz} \begin{cases} [1, 1, 1]^\top & \text{if } \mathbf{f} = 0 \text{ and } \dot{\boldsymbol{\theta}} \neq \boldsymbol{\omega} \\ \mathbf{f} & \text{else} \end{cases}\end{aligned}\quad (12)$$

The *signum function* $\text{sgn}(\cdot)$ returns the sign of the argument, or 0 if the argument is zero. This ensures that the only invariant state is the target velocity $\dot{\boldsymbol{\theta}} = \boldsymbol{\omega}$. At all other configurations where $\dot{V}(\boldsymbol{\theta}, \dot{\boldsymbol{\theta}}, t) = 0$, the control law (12) generates a nonzero acceleration $\ddot{\theta}_i(t)$ without increasing $V(\boldsymbol{\theta}, \dot{\boldsymbol{\theta}}, t)$, and thus some rotors will change velocities.

C. Closed-Loop Multi-Actuator Position Control

Position control is possible by implementing a feedback loop around (12) with a time-varying $\omega(t)$. Given a desired position vector $\boldsymbol{\theta}_{\text{goal}}$, a PID controller can be implemented to determine $\omega(t)$ based on the position error vector, \mathbf{e} :

$$\begin{aligned}\mathbf{e}(t) &= \boldsymbol{\theta}_{\text{goal}} - \boldsymbol{\theta}(t) \\ \omega(t) &= K_p \mathbf{e}(t) + K_i \int_0^t \mathbf{e}(\tau) d\tau + K_d \frac{d}{dt} \mathbf{e}(t).\end{aligned}\quad (13)$$

Note that θ_{goal} and $\theta_i(t)$ are real numbers and are not wrapped to $[-\pi, \pi]$. The three gain parameters may be set to achieve application-specific requirements. In simulations, $[K_p, K_i, K_d] = [10, 0, 0]$ and $\mathbf{e}(t)$ is saturated to ± 50 .

Control policy (13) scales to large numbers of rotors. For example, Fig. 4 shows simultaneous convergence to prescribed angular positions for 4, 24, and 50 rotors. All show asymptotic convergence, but convergence time increases with the number of rotors. With no load there is asymptotic convergence, but a non-zero load oscillates about $\boldsymbol{\theta}_{\text{goal}}$ because not all final configurations can be statically held by a constant gradient field. The simulated dynamic parameters used in (3) are below:

$$\begin{aligned}r_{\text{sphere}} &= 6\text{mm} & \tau_{f_i} &= 7 \times 10^{-5} \text{Nm} \\ m_{\text{sphere}} &= 7.7\text{g} & b_i &= 1 \times 10^{-7} \text{Nms/rad} \\ r_i &= 18\text{mm} & J_i &= 2m_{\text{sphere}} r_i^2 \text{kgm}^2\end{aligned}$$

The load torques τ_{ℓ_i} are set $\pm 1 \times 10^{-5} \text{Nm}$ with a random half set negative and the rest positive. These MATLAB simulations are available online [9].

III. MULTI-ACTUATOR DESIGN CONSTRAINTS

The preceding section demonstrated how closed-loop control can independently control multiple rotors. Given this capability, there are constraints that must be respected when designing an MRI powered and controlled multi-actuator

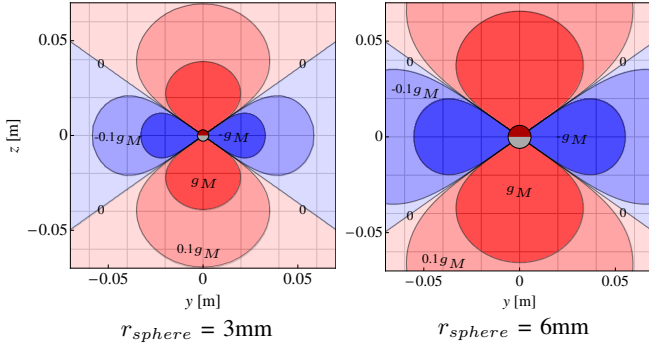


Fig. 5. One ferrous sphere in a 3T magnetic field exerts a force \mathbf{F} on an identical sphere. The contour lines show $\mathbf{F} \cdot \mathbf{n}_{12}$, the force component radially outward from the sphere at $(0,0)$ compared to the maximum force provided by the gradient coils g_M . This force is attractive (red) along the z -axis and repulsive (blue) perpendicular to z . The magnetic field is symmetric about the z -axis. If two spheres move within the dark red region, they cannot be separated using the gradient field.

system. These involve (1) arranging the rotors to minimize interaction forces, (2) MRI imaging-based tracking of each rotor, (3) geometrically arranging the rotor axes to maximize torque, and (4) calculating the stall torque as a function of the number of actuators. Each of these is described below.

A. Actuator Interaction Forces

Any ferrous material placed in the magnetic field of an MR scanner becomes a strong magnetic dipole. With multiple MR-powered motors, these dipoles exert forces on each other. Dipole forces overpower MRI gradient forces if rotors are closer than a threshold distance.

The magnetic field at position \mathbf{r}_2 generated by a spherical magnet at position \mathbf{r}_1 with magnetization \mathbf{m}_1 is [10]

$$\mathbf{B}_{\mathbf{r}_1}(\mathbf{r}_2) = \frac{\mu_0}{4\pi} \frac{3\mathbf{n}_{12}(\mathbf{n}_{12} \cdot \mathbf{m}_1) - \mathbf{m}_1}{|\mathbf{r}_2 - \mathbf{r}_1|^3}, \quad (14)$$

with $\mathbf{n}_{12} = (\mathbf{r}_2 - \mathbf{r}_1)/|\mathbf{r}_2 - \mathbf{r}_1|$. This is the *magnetic field of a dipole*. The force applied to a dipole at \mathbf{r}_1 with magnetic moment \mathbf{m}_1 by another dipole at \mathbf{r}_2 with magnetic moment \mathbf{m}_2 is approximated by

$$\mathbf{F}_{12} \approx \frac{3\mu_0}{4\pi} \frac{1}{|\mathbf{r}_2 - \mathbf{r}_1|^4} \left[5\mathbf{n}_{12} \left((\mathbf{m}_1 \cdot \mathbf{n}_{12})(\mathbf{m}_2 \cdot \mathbf{n}_{12}) \right) - \mathbf{n}_{12}(\mathbf{m}_2 \cdot \mathbf{m}_1) - \mathbf{m}_1(\mathbf{m}_2 \cdot \mathbf{n}_{12}) - \mathbf{m}_2(\mathbf{m}_1 \cdot \mathbf{n}_{12}) \right].$$

Figure 5 shows contour plots for the magnetic force exerted by two identical spheres on each other. The contour lines are drawn at $\mathbf{F}_{12} \cdot \mathbf{n}_{12} = g_M \cdot \{-1, -\frac{1}{10}, 0, \frac{1}{10}, 1\}$. Rotors with spheres closer than the g_M contour lines will become stuck because they experience a force greater than what the gradient can exert. The maximum force is along the z -axis, and the critical distance when the attractive force becomes greater than the maximum gradient force is $\sqrt[4]{\frac{2M_s\mu_0r_{sphere}^3}{g_M}}$. This interaction decays quickly and at distance $\approx 5.4r_{sphere}^{3/4}$ is 10% of the maximum gradient. The required distance, d , to ensure dipole-dipole forces are less than some *percentage* of the maximum gradient is given by

$$d \geq \sqrt[4]{\frac{2 \frac{100}{percentage} M_{sz}\mu_0r_{sphere}^3}{g_M}}. \quad (15)$$

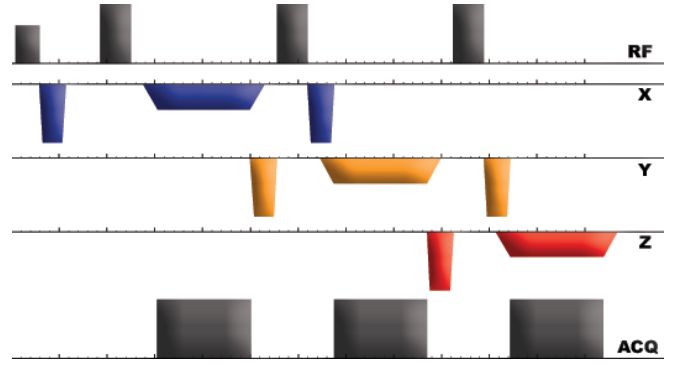


Fig. 6. MRI Fast Spin Echo sequence for tracking three orthogonal rotors.

B. Simultaneous Tracking of Multiple Rotors

An MR scanner can provide both power and feedback sensing for closed-loop motor control. Though ferrous spheres cannot be imaged with an MR scanner, a sphere can be used to selectively discriminate the resonance frequency of a fiducial marker placed a set distance from the sphere.

This method was used in [5] to track a single rotor. Attaching the fiducial marker to the same axle as the ferrous sphere, with an axial offset as shown in Fig 2, allows use of a single, configuration-independent RF-frequency to image the marker. To image a marker, the offset resonance frequency of the excitation Radio Frequency (RF) pulse is

$$\Delta f(d) = \frac{\gamma B_z(d)}{2\pi} \quad (16)$$

Here, Δf [Hz] is the RF offset, $\frac{\gamma}{2\pi}$ is the gyromagnetic ratio where γ is 42.57MHz/T, and $B_z(d)$ is the magnitude in Tesla of the magnetic field induced by the ferrous sphere at distance d from the marker. Real-time 2D tracking of the rotor is accomplished by first acquiring two orthogonal projections, and then using a peak detection algorithm to locate the marker.

Localizing several rotors is difficult because their projections can overlap. One method to avoid overlapping signals uses unique distances between marker and ferrous sphere on each rotor. By appropriate choice of offset resonance frequency and its bandwidth, only one rotor at a time is visible on any acquired projection. However, this method requires an additional tracking sequence for each rotor.

A faster alternative is to design the rotors and projections so the paths of the markers do not intersect in any projection. In this way, n rotors can be simultaneously tracked with a single acquisition sequence, followed by detecting n non-intersecting peaks on each projection. This approach is illustrated in Fig. 6, showing three orthogonal projections for tracking three orthogonal rotors. This tracking sequence requires 25ms, enabling real-time positioning of the rotors. For this method to work, each marker must be disjoint in at least two non-parallel projections, and these projections must not be parallel with the axis of rotation. Reconstructed rotor positions from an experiment with three parallel rotors are depicted in Fig. 7.

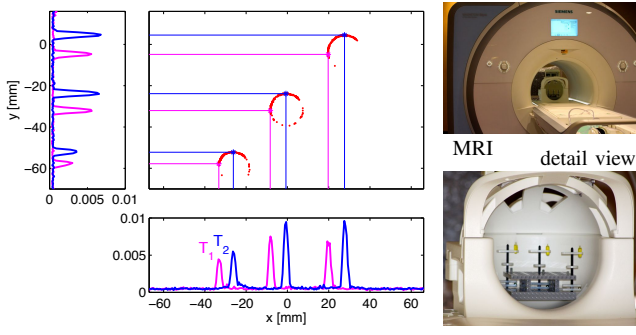


Fig. 7. Simultaneous tracking of three rotors with two line scans.

C. Optimal Geometric Arrangement of n Rotors

Controllability depends on both the geometric arrangement and the physical properties of the rotors, e.g. $\theta_i(0), r_i, v_i$. Because the physical properties are chosen to meet torque requirements, this section focuses on maximizing controllability via arranging the rotor axes of rotation.

Controller (12) exploits inhomogeneity between motor rotors. Inhomogeneity is maximized geometrically when the axes' orientations are *well spaced*, that is all axes are as far from being parallel as possible. Section III-D shows that well-spaced axes maximize output torque. Fortunately, if the rotors are arranged on the surface of a hemisphere, well-spaced axes are also maximally separated. This minimizes the dipole-dipole forces described in Sec. III-A.

This problem is a variant of the Thomson problem [11] which determines the minimum energy configuration for n electrons confined to the surface of a sphere. In this variant, to each of the n electrons located at $\mathbf{a}_i \in \mathbb{R}^3, \|\mathbf{a}_i\|_2 = 1$, an additional electron at $-\mathbf{a}_i$ is bound, and the system is solved to minimize the total energy. As in the original Thomson problem, minimal energy configurations can be rigorously identified in only a handful of cases. Instead, as in [12], this paper uses numerical optimization methods to find locally optimal solutions.

The optimization problem is

$$\begin{aligned} & \underset{\mathbf{a}_1, \mathbf{a}_2, \dots, \mathbf{a}_n}{\text{minimize}} \sum_{i \neq j} \frac{1}{\|\mathbf{a}_i - \mathbf{a}_j\|_2^2} + \frac{1}{\|\mathbf{a}_i + \mathbf{a}_j\|_2^2} \\ & \text{subject to } \mathbf{a}_i \in \mathbb{R}^3, \|\mathbf{a}_i\|_2 = 1, 1 \leq i \leq n. \end{aligned} \quad (17)$$

Both the objective function and the constraints are non-convex, but (17) can be reformulated as an unconstrained problem by changing to a spherical coordinate system parameterized by azimuth λ and elevation ϕ :

$$x = \cos(\phi) \sin(\lambda), \quad y = \cos(\phi) \cos(\lambda), \quad z = \sin(\phi).$$

The original problem had $3n$ variables and n constraints. Using spherical coordinates results in $2n$ variables and no constraints. Using the shorthand $c_\theta = \cos(\theta), s_\theta = \sin(\theta)$, the objective function (17) can be recomputed as

$$f = \sum_{j=1}^n \sum_{i=1}^j \frac{1}{2(1 - c_{\phi_i} c_{\phi_j} c_{\lambda_i - \lambda_j} - s_{\phi_i} s_{\phi_j})} + \frac{1}{2(1 + c_{\phi_i} c_{\phi_j} c_{\lambda_i - \lambda_j} + s_{\phi_i} s_{\phi_j})}, \quad (18)$$

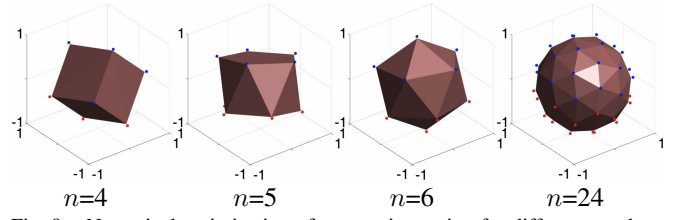


Fig. 8. Numerical optimization of rotor axis spacing for different numbers of axes, n . The rotation axes are defined by lines from each blue vertex through the origin to the corresponding red vertex. Arrangements from left to right: cube, pentagonal antiprism, icosahedron, and irregular.

and the gradient calculated as

$$\begin{aligned} \frac{\partial f}{\partial \phi_i} &= \frac{c_{\phi_i} c_{\lambda_i - \lambda_j} s_{\phi_i} - c_{\phi_i} s_{\phi_j}}{2(1 - c_{\phi_i} c_{\phi_j} c_{\lambda_i - \lambda_j} - s_{\phi_i} s_{\phi_j})^2} + \\ & \quad \frac{c_{\phi_i} c_{\lambda_i - \lambda_j} s_{\phi_i} - c_{\phi_i} s_{\phi_j}}{2(1 + c_{\phi_i} c_{\phi_j} c_{\lambda_i - \lambda_j} + s_{\phi_i} s_{\phi_j})^2} \\ \frac{\partial f}{\partial \lambda_i} &= \frac{c_{\phi_i} c_{\phi_j} s_{\lambda_i - \lambda_j}}{2(1 - c_{\phi_i} c_{\phi_j} c_{\lambda_i - \lambda_j} - s_{\phi_i} s_{\phi_j})^2} + \\ & \quad \frac{c_{\phi_i} c_{\phi_j} s_{\lambda_i - \lambda_j}}{2(1 + c_{\phi_i} c_{\phi_j} c_{\lambda_i - \lambda_j} + s_{\phi_i} s_{\phi_j})^2}. \end{aligned} \quad (19)$$

MATLAB code implementing gradient descent on (18) using (19) to find locally optimal solutions is available at [13]. Example output is shown in Fig. 8.

D. Stall Torque versus Number of Actuators

Two effects must be considered when computing stall torque. The first is related to the directionality of the maximum gradient that can be produced by a scanner. The magnetic gradients in the three coordinate directions are produced by three separate coils and amplifiers. The maximum gradient that can be applied in each direction depends on the maximum current that each coil is designed to handle. The practical implication is that the maximum gradient that can be generated is not directed along one of the three principal coordinate axes, but occurs off-axis when the three gradient coils are all producing their maximum values. The result is that, for any given rotor axis, the maximum torque varies cyclically with rotation angle.

The second effect arises because control effort must be divided among many rotors. This section analyzes the average torque produced with 1, 2, 3, or n rotors and how geometrically arranging the rotor axes modifies this torque.

a) Single rotor: Consider one rotor aligned along the MRI x -axis. The state is $[\theta_x, \dot{\theta}_x]^T$. Actuating the F_y and F_z gradient fields imparts a torque on this rotor. This analysis compares the *stopped torque*, the torque applied to a stationary rotor, assuming without loss of generality that the velocity error is +1. After setting the maximum gradient, rotor length, saturation magnetization, and inertia to 1, the stopped torque under control law (11) as a function of θ_x is

$$\tau_x = \text{sgn}(c_{\theta_x}) c_{\theta_x} + \text{sgn}(s_{\theta_x}) s_{\theta_x}. \quad (20)$$

Integrating (20) over θ_x produces an average torque of $\frac{4}{\pi} \approx 1.27$ Nm. Equation (20) is plotted in Fig. 9. The three MRI gradients can be independently maximized. This can be exploited by picking a rotor axis such that each gradient

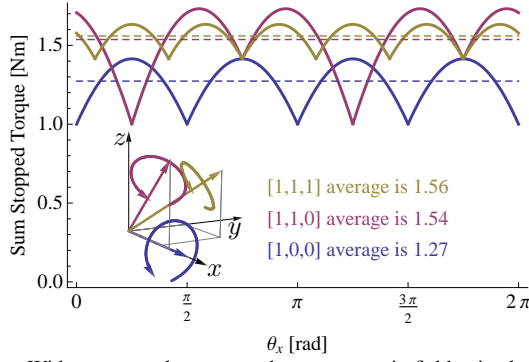


Fig. 9. With one rotor that rotates about a magnetic-field axis, the average stopped torque is $\frac{4}{\pi}$, with minimum 1 and maximum $\sqrt{2}$. Rotating about the vector $[1, 1, 0]$ or $[1, 1, 1]$ generates slightly larger average torques.

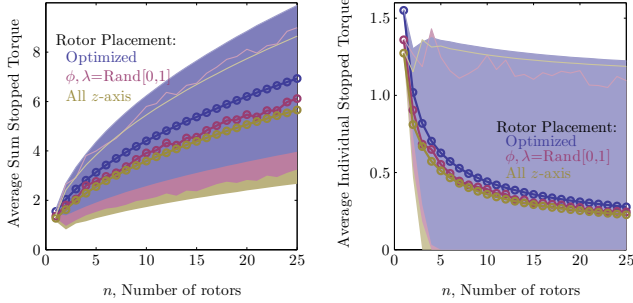


Fig. 10. Average stopped torque as a function of the number of rotors n for three different axes placement strategies. The sum torque increases sublinearly with n . The scale is normalized so 1 is the maximum torque a single gradient could impart on one rotor. Mean and \pm one standard deviation are plotted. The *optimized* placement strategy has the highest average torque. A rotor spinning around the axis $[1,1,0]$ or $[1,1,1]$ generates larger average torques than $[1,0,0]$.

b) *Two rotors*: For multiple rotors, the average torque is calculated by dividing the sum stopped torque of all the rotors by the number of rotors. With two orthogonal rotors oriented along the MRI x and y axes, each rotor torque averages $\frac{2+\pi}{2} \approx 1.04\text{Nm}$.

c) *Three rotors*: With three orthogonal rotors oriented along the MRI x, y , and z axes, the torques produced are

$$\begin{aligned}\tau_x &= \text{sgn}(c_{\theta_x} - s_{\theta_y})c_{\theta_x} + \text{sgn}(s_{\theta_x} - c_{\theta_z})s_{\theta_x} \\ \tau_y &= \text{sgn}(c_{\theta_y} - s_{\theta_z})c_{\theta_y} + \text{sgn}(s_{\theta_y} - c_{\theta_x})s_{\theta_y} \\ \tau_z &= \text{sgn}(c_{\theta_z} - s_{\theta_x})c_{\theta_z} + \text{sgn}(s_{\theta_z} - c_{\theta_y})s_{\theta_z} \\ \bar{\tau}_3 &= \frac{1}{3} \frac{1}{(2\pi)^2} \int_0^{2\pi} \int_0^{2\pi} \int_0^{2\pi} \tau_x + \tau_y + \tau_z \, d\theta_x \, d\theta_y \, d\theta_z.\end{aligned}\quad (21)$$

Each rotor averages a stopped torque of $\bar{\tau}_3 = \frac{8}{\pi^2} \approx 0.81$.

d) *n rotors*: With n rotors, the average stopped torque is calculated by integrating over each angle θ_i and dividing by n :

$$\bar{\tau}_n = \frac{1}{n} \frac{1}{(2\pi)^n} \underbrace{\int_0^{2\pi} \dots \int_0^{2\pi}}_n \sum_{i=1}^n \tau_i \, d\theta_1 \dots d\theta_n \quad (22)$$

This integral is difficult to evaluate, so Monte Carlo simulations are used to estimate the integral. Every data point in Fig. 10 is the result of 10^6 simulations. Three methods for orienting rotors are compared:

- *Optimized*: using the numerical optimization from Section III-C generates the largest average stopped torque.

- *Random*: in spherical coordinates, the azimuth and orientation of the rotor axis are set uniformly randomly in $[0,1]$. This setup produces lower average torque and erratic variance values.
- *All z-axis*: sets all rotor axis to $[0,0,1]$. This arrangement has no inhomogeneity. However, the system is controllable as long as the rotors have different initial orientations: $\theta_i(0) \neq \theta_j(0) \, \forall i, j \in [1, n]$. This method results in the lowest average torque.

IV. CASE STUDY: A THREE-AXIS BIOPSY ROBOT

To study the preceding topics in the context of a practical example system, a three-axis biopsy robot powered by DC motors is considered [6]. Figure 1 is a schematic of the proposed system. The system has a fixed base that is attached to the patient. Two actuators, θ_x and θ_y , control orthogonal axes of a nested spherical yoke. A carriage rides along the intersection of this yoke. Mounted on this carriage is a third actuator, θ_{needle} , that can insert a needle through a pivot point at the center of the base. The original design allows θ_x and θ_y to rotate between $[-\pi/6, \pi/6]$, and inserts θ_{needle} from $[0,100]\text{mm}$, resulting in a spherical quadrilateral workspace with volume $(\theta_{needle})^3\pi/9$. The base has diameter 100mm, and the nested yokes have radii 50mm.

a) *Maximizing Torque*: The rotors attached to the spherical yokes are subject to a torque due to gravity, τ_{mass} , and a needle-depth dependent torque, τ_{needle} , as well as the frictional torques in (3).

$$\begin{aligned}\tau_{mass} &= mg\ell \sin(\theta_i) \quad [\text{Nmm}] \\ \tau_{needle} &= \theta_{needle} \frac{60}{100} \quad [\text{Nmm}]\end{aligned}\quad (23)$$

The lumped mass g of the carriage and needle actuator is 0.1kg and the yoke radius $\ell=50\text{mm}$ [6]. The frictional losses in the gear train are represented by $\eta_e \in [0,1]$, a dimensionless parameter for motor efficiency.

The two yoke actuators require 100Nmm of torque and the needle actuator requires 50Nmm of torque. Assuming a conservative $\eta_e = 0.5$, with a gear reduction ratio G , the motor torque is

$$\tau_{motor} = \eta_\tau \eta_e G r_i \frac{4}{3} \pi r_{sphere}^3 M_{sz} g_M. \quad (24)$$

Here η_τ is the average torque per rotor for $n = 3$ rotors, which was evaluated as ≈ 0.81 in Section III-D. Using a rotor radius of $r_i=20\text{mm}$ and a sphere radius $r_{sphere}=6\text{mm}$, the yoke actuators require a gear reduction of $G_{xy}=250$, and the needle actuator requires $G_n=125$.

b) *Minimize Actuator Interaction Forces*: The ferrous spheres must be separated to minimize dipole-dipole forces, as described in Section III-A. According to (15), to limit dipole-dipole forces to less than 10% of maximum gradient forces with 6mm radius ferrous spheres requires at least 116mm spacing. Several candidate designs are shown in Fig. 11. Orienting the needle actuator along the $[-1,-1,0]$ axis resulted in the smallest form factor, with an axial offset of 75mm on each rotor.

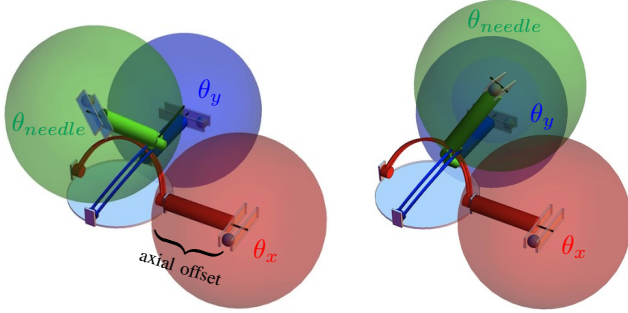


Fig. 11. Candidate designs and dipole-interaction. Spheres represent minimum separation constraint. The design at right violates the constraint.

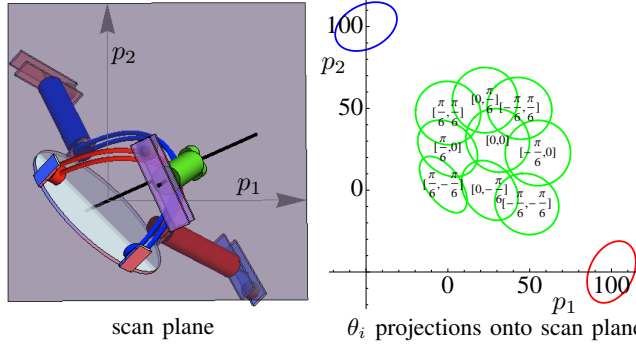


Fig. 12. All three rotors can be localized with two orthogonal line scans. These line scans can be selected such that the ellipses parameterized by θ_i are disjoint for all configurations $[\theta_x, \theta_y]$.

c) Simultaneous Rotor Tracking: For fast real-time control, the rotors must be arranged to minimize the number of line scans needed to localize the markers, as described in Section III-B. If the markers are placed 25mm axially inward from the ferrous spheres, then the position of each rotor can be detected with just two line scans, as shown in Fig. 12. The projections along $p_1=[-1,2,2]$ and $p_2=[2,-1,2]$ are orthogonal, and result in ellipses for all values of $[\theta_x, \theta_y] \in [-\pi/6, \pi/6]$. Moreover, the projections for the three rotors are disjoint in both p_1 and p_2 .

d) Simulation: The biopsy robot design was simulated with an input sequence comprised of four step-input commands: 1) move the carriage to full extent $[\theta_x, \theta_y] = [-\pi/6, \pi/6]$, 2.) insert the needle 100 mm, 3.) retract the

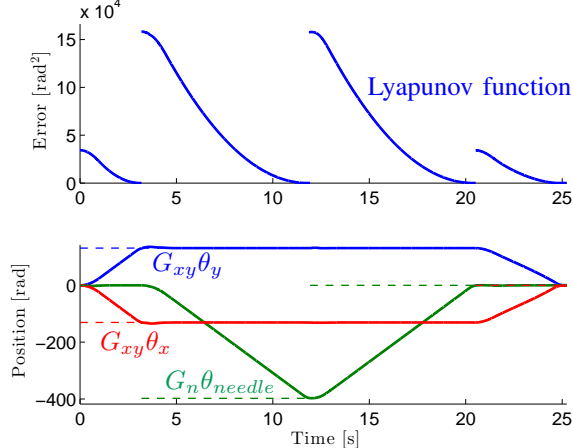


Fig. 13. Simulation with a three-rotor biopsy robot: moving the carriage to full extent $[\theta_x, \theta_y] = [-\pi/6, \pi/6]$, inserting the needle 100 mm, then retracting the needle and finally returning to $[\theta_x, \theta_y] = [0, 0]$.

needle 4.) return to $[\theta_x, \theta_y] = [0, 0]$. Fig. 13 shows the sum squared error and position traces during these four movements. The system response for all steps is smooth.

V. CONCLUSION

MRI-based multi-rotor control poses both control-theoretic challenges and practical implementation issues. To address these, this paper has provided an optimization scheme for rotor placement and derived a globally asymptotically stabilizing controller for n actuators. Both a velocity controller (12) and a position controller (13) were implemented. MATLAB implementations of these controllers are available at [9].

These controllers exploit inhomogeneities in rotor axis orientation. Constructing motors with axes that are not parallel requires careful balancing of the rotor shafts. However, it is not necessary for the rotors to be non-parallel. Ongoing research indicates that the proposed control law can also stabilize parallel rotor shafts using other inhomogeneities, e.g. $r_i, \theta_i(0), v_i$. If all axes are parallel to the gravity vector, gravity no longer interferes with rotor movement. This makes counterweights unnecessary, and allows using extremely low-friction jewel bearings since axles are not under radial load.

REFERENCES

- [1] M. Ho, A. B. McMillan, J. M. Simard, R. Gullapalli, and J. P. Desai, "Towards a meso-scale SMA-actuated MRI-compatible neurosurgical robot," *IEEE Transaction on Robotics*, vol. 28, no. 1, pp. 213–222, 2012.
- [2] G. S. Fischer, A. Krieger, I. Iordachita, C. Csoma, L. L. Whitcomb, and G. Fichtinger, "MRI compatibility of robot actuation techniques—a comparative study," in *Medical Image Computing and Computer-Assisted Intervention—MICCAI 2008*. Springer, 2008, pp. 509–517.
- [3] S. Martel, J.-B. Mathieu, O. Felfoul, A. Chanu, E. Aboussouan, S. Tamaz, P. Pouponneau, L. Yahia, G. Beaudoin, G. Soulez, and M. Mankiewicz, "Automatic navigation of an untethered device in the artery of a living animal using a conventional clinical magnetic resonance imaging system," *Applied Physics Letters*, vol. 90, no. 11, pp. 114 105–114 105–3, Mar 2007.
- [4] P. Vartholomeos, L. Qin, and P. E. Dupont, "MRI-powered actuators for robotic interventions," in *IEEE Int. Rob. and Sys.*, 2011, pp. 4508–4515.
- [5] P. Vartholomeos, C. Bergeles, L. Qin, and P. E. Dupont, "An MRI-powered and controlled actuator technology for tetherless robotic interventions," *Int. J. Rob. Res.*, vol. 32, no. 13, pp. 1536–1552, 2013.
- [6] C. J. Walsh, "Image-guided robots for dot-matrix tumor ablation," Ph.D. dissertation, Massachusetts Institute of Technology, Massachusetts Institute of Technology, Dept. of Mechanical Engineering, 2010. [Online]. Available: <http://hdl.handle.net/1721.1/61613>
- [7] Z. Artstein, "Stabilization with relaxed controls," *Nonlinear Analysis*, vol. 15, no. 11, pp. 1163–1170, 1983.
- [8] A. Becker, C. Onyuksel, and T. Bretl, "Feedback control of many differential-drive robots with uniform control inputs," in *IEEE/RSJ International Conference on Intelligent Robots and Systems (IROS)*, Vilamoura, Portugal, Oct. 2012, pp. 2256–2262.
- [9] A. Becker. (2014, Jan.) "Control n MRI-powered actuators." MATLAB Central File Exchange. [Online]. Available: <http://www.mathworks.com/matlabcentral/fileexchange/45331>
- [10] R. Schill, "General relation for the vector magnetic field of a circular current loop: a closer look," *Magnetics, IEEE Transactions on*, vol. 39, no. 2, pp. 961–967, Mar 2003.
- [11] J. J. Thomson, "On the structure of the atom: an investigation of the stability and periods of oscillation of a number of corpuscles arranged at equal intervals around the circumference of a circle; with application of the results to the theory of atomic structure," *Philosophical Magazine Series 6*, vol. 7, no. 39, pp. 237–265, Mar. 1904.

- [12] H. Peng and Y. Yu, "Optimization on the surface of the (hyper)-sphere," Purdue University, Tech. Rep., May 2012. [Online]. Available: <https://www.cs.purdue.edu/homes/pengh/reports/5900P.pdf>
- [13] A. Becker. (2013, Nov.) "Generate Non-Parallel Axes." MATLAB Central File Exchange. [Online]. Available: <http://www.mathworks.com/matlabcentral/fileexchange/44515>